SLAC-PUB-3384
July 1984
(N)

ELECTROMAGNETIC SHOWER DEVELOPMENT AND APPLICATIONS TO SAMPLING CALORIMETERS*

Charles Y. Prescott
Stanford Linear Accelerator Center
Stanford University, Stanford, California 94305

1. Introduction

The application of electromagnetic theory to particle interactions is an old subject which represented one of the early successes in the study of particle interactions and fundamental forces. The ability to describe properties of electron, positron, and photon interactions has led to applications in numerous experimental devices used in high energy experiments. The subject is now considered to be relatively mature, but applications continue to evolve as new ideas are tried and new techniques become available. This report is a review of the underlying processes, a discussion of the application to electromagnetic calorimetry, discussions of some scaling laws and approximations that serve to guide designs of experimental devices, and examples where these principles are put to work.

2. Electromagnetic Shower Theory

The processes of interest in cascades of high energy electrons, positrons, and photons have long been understood. These processes are the mechanisms by which energy from incoming primary electrons, positrons, or photons can transfer energy to an absorbing medium. These energy loss mechanisms include excitation of atomic levels, ionization of atoms, collisions with atomic electrons, radiation of photons (also called bremsstrahlung), and pair production of electron-positron pairs. Not considered in the electromagnetic theory are other processes such as production of hadrons, pair production of muons, or or weak processes. These can be shown to be negligible for most considerations. Generally each of the fundamental processes can be calculated exactly; the theory of quantum electrodynamics is well understood. In practice, the application of these fundamental processes to the interaction with materials is best described through suitable simplifications and approximations which deal with parameters of the materials. Validity of some of the formulae may be limited. In spite of these limitations, however, the usefulness of various approximate formulations make designing detectors simpler.

---

* Work supported by the Department of Energy, contract DE-AC03-76SF00515.

Invited talk presented at the First Workshop on Colliding Beam Physics in China, Beijing, People Republic of China, June 12-21, 1984.

Figure 1 shows the fundamental processes of interest. The electromagnetic shower includes these fundamental processes and others. Collision of charged particles with atomic electrons leads to ionization of the atoms. Collisions of photons with atomic electrons with the subsequent emission of an electron is called the photoelectric effect. The ejection of an electron with the scattered photon occurs through the Compton effect. Deflection of charged particles in the Coulomb field of the nucleus contributes to the scattering ("single" for one scatter, "plural" for several scatters, or "multiple" for many scatters). High energy photons can interact with the nuclei yielding positron-electron pairs, and positrons can scatter from electrons (Bhabha scattering).

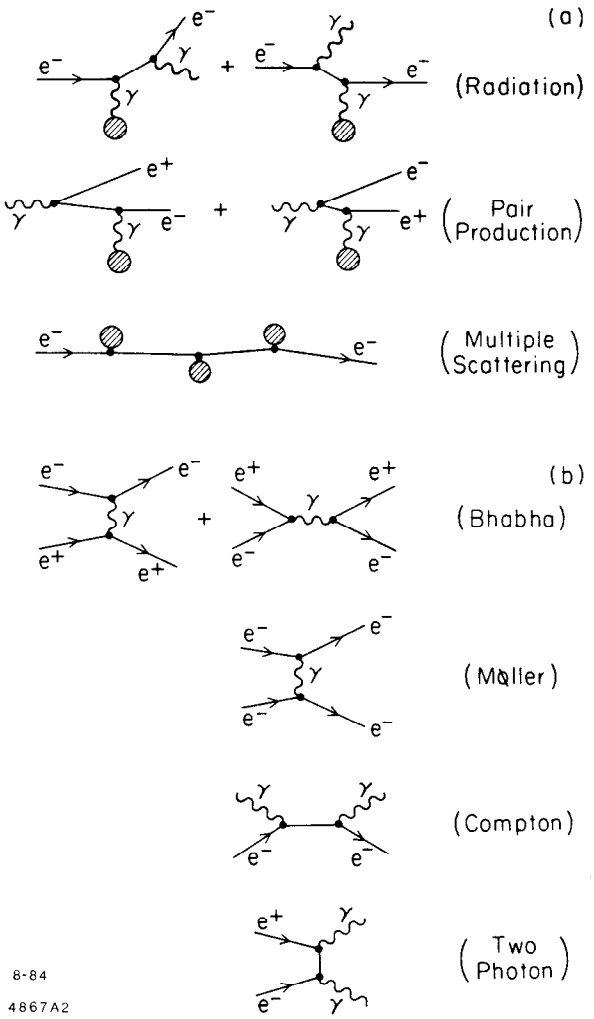

Figure 1. The primary processes which are responsible for electromagnetic shower development: (a) Interactions with the nucleus; and (b) Interactions with atomic electrons.

(a) Interactions with nuclei

(i) Radiation

Radiation is the emission of energy in the form of photons by an electron in the Coulomb field of a nucleus. Let $P(E,k)dk\ dx$ be the probability for an electron of energy E traversing a material of thickness dx gm/cm^2 to emit a photon of energy k in the interval dk. Then $P(E,k)$ has the form[1]

$$P(E,k)dk = 4\alpha N_0 (Z^2/A)\, r_e^2 \left(\frac{dk}{k}\right) F(E,k/E)$$

where $\alpha = 1/137$, N_0 is Avogadro's Number 6.023×10^{23}, Z and A are respectively the nuclear charge and weight, r_e is the classical electron radius, and F is a smoothly varying function. The average energy loss per gm/cm^2 by radiation is defined to be

$$k_{rad}(E) = \int_0^E k\, P(E,k)\, dk$$

and has the form

$$k_{rad}(E) = 4\alpha N_0 (Z^2/A)\, r_e^2\, E \left[\ell n(183 Z^{-\frac{1}{3}}) + \frac{1}{18}\right].$$

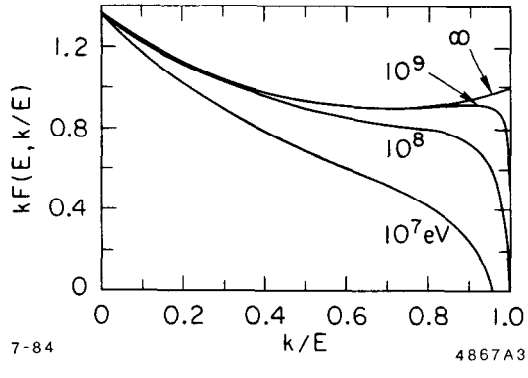

Figure 2. The normalized photon energy spectrum $k\,P(E,k)\,X_0$ versus k/E for *lead*. The numbers attached to the curves refer to the total energy of the electrons (from Ref. 1).

It follows that

$$\Delta E/E \approx \Delta t$$

where Δt is the thickness $\Delta x/X_o$ and

$$1/X_o \approx 4\alpha N_o(Z^2/A)\, r_e^2\, \ell n(183Z^{-\frac{1}{3}}).$$

The quantity X_o is the "radiation length" of the material, and sets the length scale for the radiating medium. In different materials shower development is similar when expressed in units of radiation lengths. Figure 2 shows the normalized radiated photon spectrum for the common material lead.

For mixtures of materials, the combined radiation length is obtained from

$$1/X_o = p_1/X_1 + p_2/X_2 + ...$$

where $p_1, p_2, ...$ represent the fractional weights of the constituent materials of radiation lengths $X_1, X_2, ...$ respectively.

The angle of emission of the photon relative to the incident electron is approximately given by[1]

$$\theta_{rms} \approx m_e c^2\, \ell n(E/m_e c^2)/E$$

which for high energy electrons is peaked in a very narrow cone about the incident electron. At energies below a few MeV, however, the emission of photons can occur at wider angles. Thus in electromagnetic showers, the particles seen at wide angles and distances from the shower core tend to be low in energy.

(ii) Pair production

Pair production is the main energy loss mechanism for high energy photons. This process occurs in the Coulomb field of the nucleus. The photon must have the the threshold energy $2m_e c^2$ for this process to occur. The probability for a high energy photon of energy k to produce a positron of energy E' in the interval dE' is[1]

$$P(k, E')dE'\, dx = 4\alpha N_o(Z^2/A)\, r_e^2\, (dE'/E')\, G(k, E'/k)\, dx$$

where $G(k, E'/k)$ is a well-behaved function. The normalized energy spectrum for the positrons is shown in Figure 3. This spectrum is symmetric about $E' \approx k/2$ with a dip in the midpoint that is most pronounced at the highest values of k.

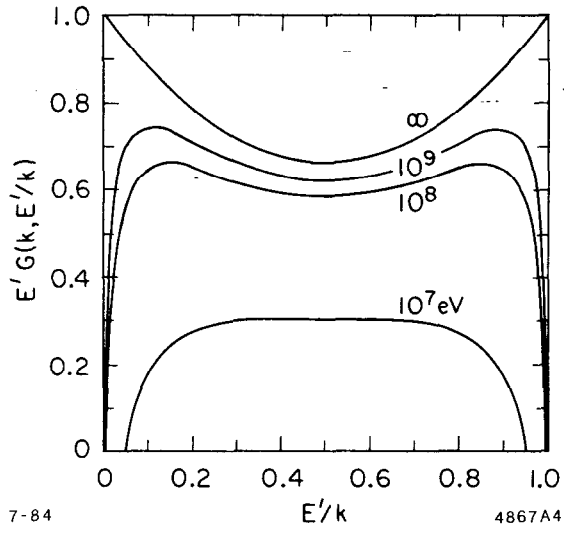

Figure 3. The differential probability of pair production per radiation length of *lead* versus E'/k, the ratio of positron energy to incident photon energy. The numbers attached to the curves refer to the incident photon energy (from Ref. 1).

(iii) Multiple Scattering

Multiple scattering of charged particles by Coulomb forces in the atoms contribute larger divergences in angle, and hence lateral spread, than do the fundamental processes. For radiating media of finite thickness, the charged particles undergo multiple Coulomb encounters, leading to a Gaussian probability in angle and displacement. The projected angular deflection can be approximated by a distribution[1]

$$Q(t,\theta_y) \approx \frac{1}{\sqrt{2\pi}\sigma_\theta} \exp(-\theta_y^2/2\sigma_\theta^2)$$

Integration of this distribution leads to the total probability

$$\int P(k,E')dE' = 4\alpha N_o(Z^2/A)\, r_e^2 \left[\frac{7}{9}\ell n(183Z^{-\frac{1}{3}}) - \frac{1}{54}\right]$$

which leads to a probability per radiation length of 7/9 (compared to unity for an electron). The comparison of Compton and pair production probabilities versus energy are shown in Figure 4. Figure 5 shows the comparison between ionization energy loss and radiation energy loss for an incident electron of energy E.

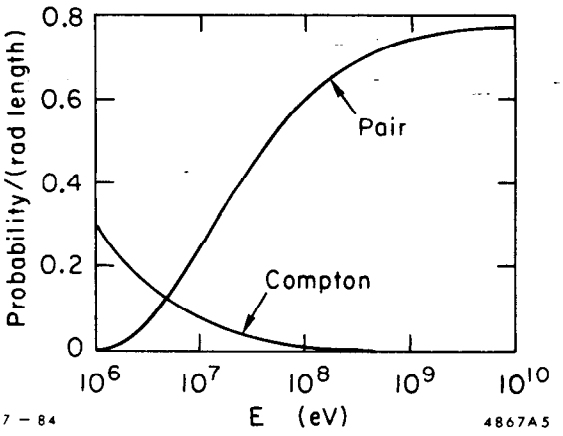

Figure 4. Comparison of probability per radiation length of *lead* for Compton scattering and pair production versus incident photon energy k (from Ref 1).

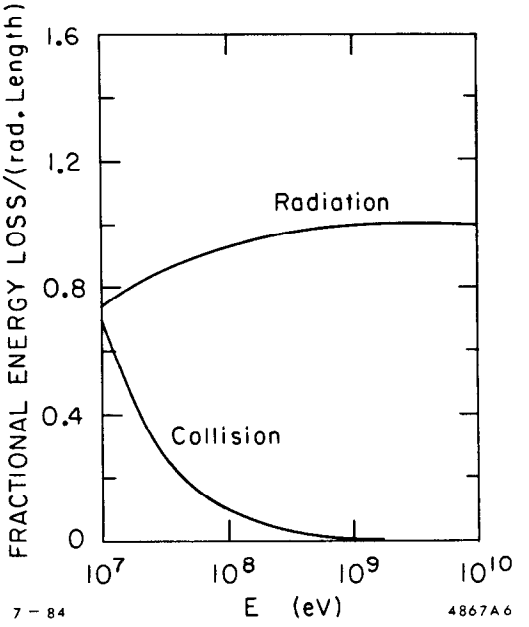

Figure 5. Comparison of fractional energy loss per radiation length of *lead* versus incident electron energy (from Ref. 1).

where $\sigma_\theta \approx E_s\sqrt{t/2}/p\beta$, p and β are the velocity and momentum in MeV, t the thickness in radiation lengths, and $E_s = m_e c^2\sqrt{4\pi/\alpha} = 21.2$ MeV. This distrubution is averaged over the displacement in y. This approximation assumes the charged

particle loses no energy during the multiple scatters in the thin material. Photons suffer no multiple scattering, since they are not influenced by the Coulomb fields.

In addition to the angular deflections, charged particles undergo displacements as well. The distribution in displacement y is given by approximately by

$$S(t,y) = \frac{1}{\sqrt{2\pi}\sigma_y} \exp(-t_y^2/2\sigma_y^2)$$

where

$$\sigma_y = \frac{E_s t^{3/2}}{\sqrt{2}p\beta} = \sigma_\theta t$$

and $t_y = y/X_o$ is the displacement in units of radiation lengths.

(b) Interactions with atomic electrons

(i) Energy loss by ionization

Energy loss by collision with atomic electrons depends on many properties and parameters, including the density of the medium, the velocity of the incident particle, the ionization potential of the atoms, and the charge Z and the weight A of the nucleus. It is customary to quote the energy loss due to ionization in units of gm/cm^2. A typical value for ionization energy loss for a minimum ionizing particle (say a cosmic ray μ^+ of high energy) is approximately 2 MeV per gm/cm^2. This energy loss, $-dE/dx$, is given by

$$k_{col}(E) = \frac{2Cm_ec^2}{\beta^2}\left[\ell n\left(\frac{\pi^2(m_ec^2)^2}{(1-\beta^2)^{3/2}I^2}\right) - 2.9\right]$$

where $C = \pi N_o(Z/A)r_e^2 = .150(Z/A)$ gm^{-1}cm^2, β is the velocity, and I is the average ionization potential of the medium. This energy loss shows a rapid decrease as β increases to a minimum around $\beta \approx 0.9$, then increases into a "relativistic rise" region. The amount of relativistic rise depends on the density of the medium, being larger for low density media such as gases, and almost nonexistent for solids. The ionization loss in gases serves as the basis for dE/dx measurements in gas drift chambers.

Materials are characterized by their primary specific ionization which is simply the average number of collisions which produce one or more free electrons per gm/cm^2 of material. The total specific ionization is the total number of free electrons produced by primary and all secondaries combined per gm/cm^2. The interesting parameter is the energy spent to produce one ion pair, typically 20 to 35 eV for a wide variety of substances[1].

Fluctuations in the energy loss mechanism can be important to devices designed to measure primary energy. The fluctuations are a statistical phenomenon. For thin

absorbers, these fluctuations can be a large fraction of the average energy loss. More importantly, these fluctuations are not Gaussian, but have relatively long tails (the "Landau tail")[1].

Scattering of positrons and electrons with atomic electrons is an important part of the standard picture of energy loss mechanisms. The scattering of positrons by electrons is called Bhabha scattering and the scattering of electrons by electrons is called Møller scattering.

(ii) Bhabha scattering

The cross section for Bhabha scattering is[2]

$$d\sigma_{Bhab}(E)/dE' = \frac{X_o n 2\pi r_e^2 m_e c^2}{(E - m_e c^2)^2}\Big[(1/\rho\beta^2 - B_1)/\rho + B_2 + \rho(\rho B_4 - B_3)\Big]$$

where n = electron density (electrons per cm^2), E is the incident positron energy, E' is the scattered electron energy, and $B_1 = 2 - y^2$, $B_2 = (1 - 2y)(3 + y^2)$, $B_3 = (1-2y)^3+(1-2y)^2$, $B_4 = (1-2y)^3$ with $y = 1/(\gamma+1)$, and $\rho = (E'-m_e c^2)/(E-m_e c^2)$.

(iii) Møller Scattering

The cross section for Møller scattering has the form[2]

$$d\sigma_{M\emptyset ll}(E)/dE' = \frac{X_o n 2\pi r_e^2 m_e c^2}{\beta^2(E - m_e c^2)}\Big[C_1 + (1/\rho - C_2)/\rho + (1/(1-\rho) - C_2)/(1-\rho)\Big]$$

where $\rho = (E'-m_e c^2)/(E-m_e c^2)$, $C_1 = ((\gamma-1)/\gamma)^2$, $C_2 = (2\gamma-1)/\gamma^2$, $\gamma = E/m_e c^2$, and E and E' are the incident and scattered electron energies respectively.

(iv) Compton scattering

Compton scattering is the interaction of photons with atomic electrons. The cross section for Compton scattering is given by[2]

$$d\sigma_{Comp}(k, k')dk' = \frac{X_o n \pi r_e^2 m_e c^2}{k^2}\Big[(C_1/\rho + C_2)/\rho + C_3 + \rho\Big]$$

where $\rho = k/k'$, $C_1 = \delta^{-2}$, $C_2 = 1-2(1+\delta)/\delta^2$, $C_3 = (1+2\delta)/\delta^2$, and $\delta = k/m_e c^2$.

This process drops rapidly as $k' \to k$ or as k becomes large.

(v) Two photon annihilation

Positrons and electrons can also annihilate into two photons with the cross section given by[2]

$$d\sigma_{2\gamma}(E)/dk = \frac{X_o n 2\pi r_e^2}{(\gamma^2 - 1)m_e c^2}\Big[S_1(k/m_e c^2) + S_1(\gamma + 1 - k/m_e c^2)\Big]$$

where $S_1(x) = (\gamma+1+2\gamma/(\gamma+1)-1/x)/x-1$ and $\gamma = E/m_e c^2$. These basic processes are the ones involved in development of showers when high energy electrons, positrons, or photons interact with atomic electrons.

3. Electromagnetic Shower Computation

Development of electromagnetic showers, or cascades, is a complicated multi-body problem. It defies any precise analytic analysis, although approximate forms have been reasonably successful. The early attempts to characterize electromagnetic showers were based on diffusion equations. Inconsistencies between calculations and experimental results led to refined attempts to describe electromagnetic shower development by computer code. The underlying quantum mechanical nature of the processes involved led to development of Monte Carlo techniques when fast computers became available[3–8]. The standard code used today to describe electromagnetic showers is called EGS (for Electron-Gamma Shower), written by Ford and Nelson at Stanford University. This code evolved over a number of years, and is well described in their manual. Unlike earlier analytic calculations, this code permits the experimenter to insert details of geometry and complex materials into the calculation. Thus modern computers and modern computer code have opened up a new tool for detailed analysis of electromagnetic showers in experimental situations.

Experimental measurements of shower development have also served to refine calculations. Development of showers in the longitudinal and lateral coordinates have been measured[9–12]. Figure 6 shows a comparison of the EGS Monte Carlo to experimental measurements of charged particle number versus radiation thickness for a 1 GeV electron-initiated shower. The calculation defines a lower cutoff, 5 MeV, below which particles are ignored. Agreement with experimental results is excellent.

4. Scaling Laws and Energy Resolution Considerations

(a) Shower leakage

The longitudinal development of a shower can be approximated by the form

$$dE/dt \approx At^{\alpha} \exp(-t/\lambda)$$

where E is the energy loss to the medium, t is the depth in radiation lengths, and α and λ are adjustable parametes. These parameters have slow (logarithmic) variation

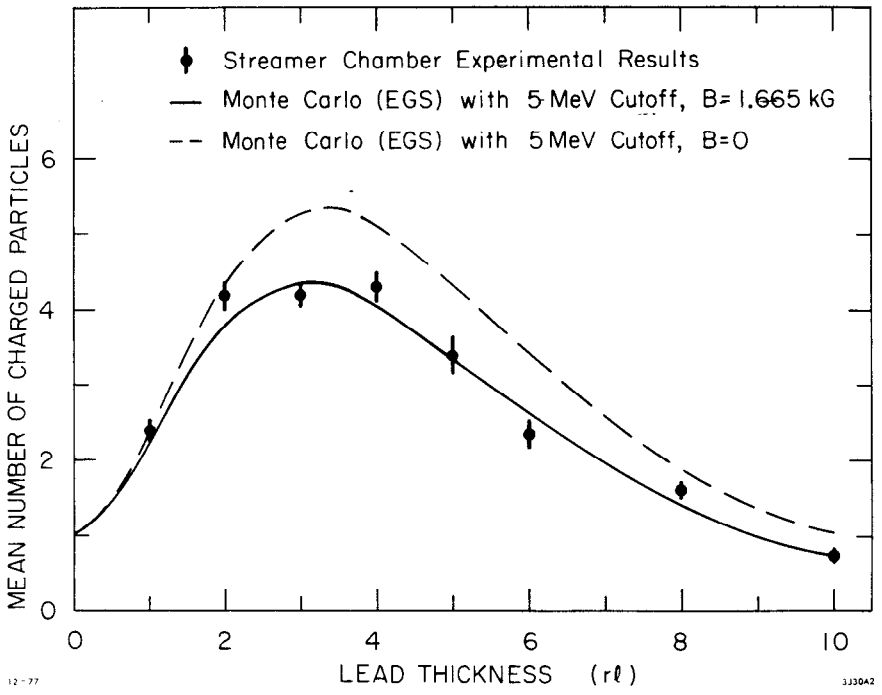

Figure 6. Comparison of experimental results with a calculation by EGS. The quantities plotted are tne mean number of charged particles above 5 MeV versus depth in radiation lengths of *lead*, for 1 GeV electrons incident (from Ref. 2).

with energy. For 1 GeV showers, the assumption of this form leads to

$$dE/dt \approx E_o t^2 \exp(-t/2)/2^4$$

where the parameter α and λ have been set to 2. This form is properly normalized to the total incident energy. For shower counters of finite thickness, energy leaks out the back, leading to undetected energy escaping and correspondingly fluctuations in the total energy energy absorbed. The fluctuations are primarily driven by the longitudinal variation in the point of first interaction. This variation , $\delta t \approx 1$, appears as a variation in the the total absorption length of approximately 1 X_o. The fluctuation in energy absorbed in a counter of thickness T is

$$\delta E \approx \delta t \times dE/dt \ (at\ t = T)$$

and

$$\sigma_L = \delta E/E_o \approx T^2 \exp(-T/2)/2^4 \ .$$

(b) Sampling fluctuations

Sampling fluctuations in sampling shower counters arise because energy losses vary in the active and passive radiator sections from one shower to the next. Active sampling media differ in shower counter designs, with scintillator, gas proportional counters, and liquid argon being common examples. The passive layers in sampling counters are usually high Z substances, with lead the most common choice. Fluctuations in resolution are estimated by considering the energy deposited in the active parts of the devices.

The total track length L is defined to be

$$L = E_o/\epsilon_o$$

where ϵ_o is the critical energy, defined as the average energy loss per radiation length for a high energy electron, and E_o is the incident energy. For lead ϵ_o has the value of 7.6 MeV. L has the units of radiation lengths. When the total shower is sampled at intervals of Δ the total number of charged particle crossings in the active samples is

$$N = L/\Delta = E_o/\Delta\epsilon_o.$$

To a good approximation these are uncorrelated, so the rms fluctuations of the energy seen in the scintillator is then

$$\sigma_{samp} \approx \delta E_{medium}/E_{medium} \approx 1/\sqrt{N} = \sqrt{\Delta\epsilon_o/E_o}$$

This relation has experimentally been verified to be valid down to $\Delta \leq .1X_o$.

(c) Noise

In addition to the fluctuations in N, the individual active detecting layer may have a "noise" associated with the measurement of energy. For photomultipliers looking at scintillator layers, this noise is the fluctuations in photoelectron n_{pe}. In sampling gas counters, the noise contribution comes from large fluctuations caused by the Landau tails in the energy deposition. In liquid argon counters, the noise is associated with the inherent noise in electronic preamplifiers.

Combining these terms leads to a sampling counter resolution given by

$$\sigma = \delta E/E_o = \sqrt{T^4 \exp(-T)/2^8 + \Delta\epsilon_o/E_o + \sigma^2_{noise}}\,.$$

Table I gives estimates of the various contributions to σ for a 1 GeV shower in a variety of sampling counter configurations.

Table I. Estimation of Sampling Calorimeter Resolution at 1 GeV

Counter Configuration	σ_L	σ_{samp}	σ_{noise}	σ_{tot}
Pb-Scintillator	%	%	%	%
$6X_0$ 12 samples	11.0	6.2	1.5(4.7)*	12.7(13.4)*
$12X_0$ 24 samples	2.2	6.2	1.5(4.7)	6.7(8.1)
$12X_0$ 48 samples	2.2	4.4	1.5(4.7)	5.1(6.8)
$20X_0$ 20 samples	0.1	8.7	1.5(4.7)	8.8(9.9)
Pb-Glass				
$6X_0$	11.0	0	5.0	12.0
$12X_0$	2.2	0	5.0	5.5
$20X_0$	0.1	0	5.0	5.0
Pb-Gas Prop. Readout				
$6X_0$ 12 samples	11.0	6.2	12.4**	17.7
$12X_0$ 24 samples	2.2	6.2	12.4**	14.0
$12X_0$ 48 samples	2.2	4.4	8.8**	10.1

*( ) for BBQ wavebar readout

** Assumes $\sigma_{\text{noise}} \simeq 2 \times \sigma_{\text{samp}}$

The various counter configurations and types have certain assumptions as follows: For scintillators with photomultipliers attached, the photoelectron statistics were estimated from the assumption of 100 photoelectrons per scintillator per track length. This will vary in different counter designs, with good designs collecting more scintillation light. Scintillator thickness, quality, light coupling, and photomultiplier quantum efficiency all contribute to the photoelectron yield. For wavebar readout of plastic scintillator counters, the light conversion is about 10% of that of a direct coupling, so the assumption for these counters was 10 photoelectrons per scintillator layer per track crossing. For lead-glass shower counters, the production of light is by Cerenkov light which results in far fewer photoelectrons. The typical good lead-glass counter sees about 400 photoelectrons per GeV of indident energy. Sampling fluctuations in lead glass are negligible, since the entire counter is the active medium. For gas proportional readout the noise contribution is large due to the large fluctuations in individual pulses. For this case, σ_{noise} was set to $2 \times \sigma_{samp}$.

Two types of counters were not considered in the previous discussion because they are special. Sodium iodide (NaI) and bismuth germanate (BGO) counters have very good energy resolution. The good resolution is the result of totally active media (no sampling fluctuations) and high light yield (no photoelectron statistics). Residual

effects come from non-uniformity in light collection throughout the volume and residual leakage of energy out the sides and back. Care in the surface preparation is important, and optical uniformity is important in these counters to maintain the good resolution. NaI and BGO counters achieve approximately 1% resolution at 1 GeV, but are costly due to the need to purify the materials and to grow crystals.

Scaling of these resolutions with energy is not generally easy. For counters sufficiently thick to contain the leakage, the general form of the remaining contributions scale approximately as

$$\sigma(E)/E_o \approx \sigma(1GeV)/\sqrt{E_o}$$

and often experimental measurements of resolution are compared with this formula, even though it is only approximate.

5. Lateral Shower Spreading

Define $U(r)$ to be the energy from an incident particle of energy E_o which falls outside a cylinder of radius r whose axis coincides with the path of an incident electron, positron or photon of energy E_o. The fraction U/E_o is predicted to decrease approximately exponentially as r increases. Analytic shower theory predicts a scaling variable, called the Molière radius r_M, given by

$$r_M = X_o E_s/\epsilon_o$$

where E_s is 21.2 MeV and ϵ_o is the critical energy (7.6 MeV for lead).

Figure 7 shows measurements of this fraction U/E_o for incident energies of 100 MeV to 1 GeV and for two materials, lead and copper[9]. The conclusions from these measurements are that to a good approximation, the radial spread is independent of energy and material when expressed in terms of the parameter r_M. An approximate numerical fit is

$$U/E_o \approx .75\ \exp(-r/.25) + .25\ \exp(-r/1.081)$$

for r in units of r_M with $r \leq 4r_M$ and E_o from 100 MeV to 1 GeV.

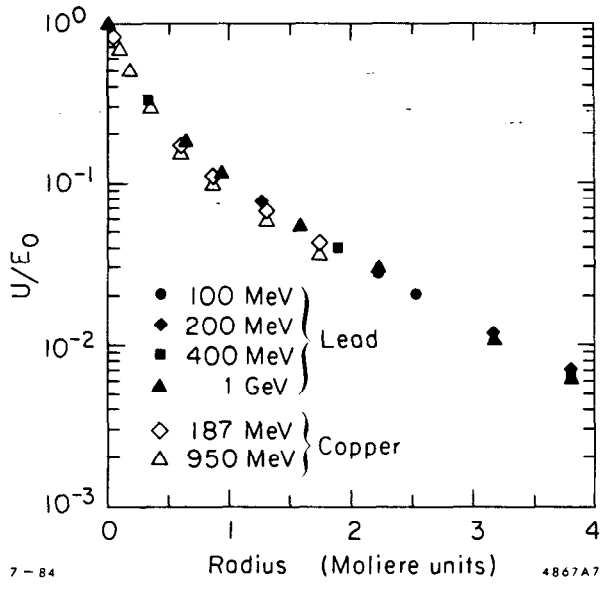

Figure 7. The fraction of energy escaping a cylinder of radius r (in Molière units) for *lead* and *copper* at energies from 100 MeV to 1 GeV (from Ref. 9).

6. Pulse Formation in Gas Calorimeters

Gas calorimeters are popular devices in large, 4π solid angle detectors for a variety of reasons including low cost, ease of construction, simplicity of gas amplification, and flexible geometries. Segmentation of the calorimeter into many small sections permits localizing of shower coordinates and measurement of energy in that localized region. The possibility of amplification in the gaseous volume reduces significantly the cost of electronics needed. Gas gains of 10^4 to 10^7 are possible, and in the latter regime, no additional electronics gain is needed; the direct pulses from sense wires can drive inexpensive digital registers. Gas mixtures vary in different applications. Typical gases used are argon-methane, argon-ethane, argon-isobutane, or argon-ethyl bromide. Table II sumarizes performances and parameters of several gas sampling calorimeters in use.

The presence of significant hydrocarbon components in the gases serves to provide heavy quenching of avalanches (i.e., to prevent propagation of pulses along anode wires via UV photons).

Pulse formation on sense wires is determined by the relatively fast electron drift inwards, followed by a relatively slow drift of the positive ions outward. When an ion pair is produced in a cell, the electron will drift to the positive electrode, the anode,

Table II. Electromagnetic Gas Calorimeters

Detector	Gas	Sample Thickness	MODE	Resolution
MAC prototype	Ar-Eth-Alcohol 49/49/1	.5 X_0	SQS	17% $/\sqrt{E}$
CDF prototype	Ar-Eth-Al 49/49/1	.5	SQS	23% $/\sqrt{E}$
Aleph prototype	Ar-Isobutane 17/83	.35		16% $/\sqrt{E}$
TPC	Ar-Ethyl Bromide 96/4	.25	Geiger	14% $/\sqrt{E}$
CLEO	Ar-CH4 91/9	.2		14% $/\sqrt{E}$
Mark III	Argon-CH4 80/20	.5	Proportional	17.5% $/\sqrt{E}$
CHARM	Argon-Isobutane 25/75	1.0		20% $/\sqrt{E}$

and the positive ion will drift to the cathode. The charge induced on the anode, at the time of electron arrival will be $e + q_A$ for each electron-ion pair, where q_A represents the induced anode charge due to the positive ion. For a single electron drifting into the anode wire where high electric fields exist, the electron will create additional ion pairs by avalanche, so that the total charge on the anode wire *per incoming electron* will be

$$Q(t) = G(e + q_A(t))$$

where G is the gas gain. The induced charge $q_A(t)$ can be calculated using an electrostatics theorem, called Green's Theorem, which states that for a set of charges q_i on a set of conductors at potentials V_i, and a second set of charges q_i' on the same conductors at potentials V_i',

$$\sum q_i V_i' = \sum q_i' V_i.$$

Applied to this problem, suppose initially charges $Q_A + q_A$, $Q_C + q_C$, and q_{ion} are on the cathode, anode, and ions respectively. Take the potentials to be V_A ,V_C, and V_{ion}. The final configuration corresponds to normal conditions Q_A, Q_C, and 0, with potentials V_A and V_C as before. Then

$$(q_A + Q_A)V_A + (q_C + Q_C)V_C + q_{ion}V_{ion} = Q_A V_A + Q_C V_C$$

or -

$$q_A V_A + q_C V_C + q_{ion} V_{ion} = 0$$

but also

$$q_A + q_C + q_{ion} = 0 \, .$$

Solving for q_A yields

$$q_A = -q_{ion}(V_{ion} - V_C)/(V_A - V_C) \, .$$

The induced charge thus depends on the the potential at the location of the ions. For proportional, saturated avalanche, of limited streamer modes, the ions form near the sense wire. The induced charges from electrons and ions initially sum to zero. When the ion eventually disappears, the final charge is Ge.

The motion of the ion is radial with velocity

$$v = dr/dt = \mu E$$

where μ is the ion mobility, and E is the electric field given by

$$E = \frac{(V_A - V_C)}{r \, \ell n(r_C/r_A)}$$

and r_C and r_A are the radii of the cathode and anode. Solving for $r(t)$ gives

$$r(t) = \sqrt{2\mu(V_A - V_C)t/\ell n(r_C/r_A) + r_C^2}$$

and

$$q_A(t) = -q_{ion}\frac{V_{ion} - V_C}{V_A - V_C} = -\frac{q_{ion}}{V_A - V_C}\int_{r(t)}^{r_C} E dr = -e\frac{\ell n(r_C/r(t))}{\ell n(r_C/r_A)} \, .$$

The total induced charge is

$$Q(t) = G(e + q_A(t)) = \frac{-e}{2 \, \ell n(r_C/r_A)} \, \ell n(t/t_i + 1)$$

where $t_i = r_A^2 \ell n(r_C/r_A)/2\mu(V_A - V_C)$. The current pulse is given by

$$i(t) = \frac{i(0)}{t/t_i + 1}$$

where

$$i(0) = \frac{Ge}{2\ \ell n^2(r_C/r_A)} \frac{2\mu(V_C - V_A)}{r_A^2}.$$

Typical proportional cells have $r_C/r_A \approx 1000$, $V_A V_C \approx 3$ kV, and $\mu \approx 1$ cm^2/Vsec. In these cells the gas gain is G. For these values of the parameters, $i(0) \approx .6$ μA for $G \approx 10^5$, and $t_i \approx 1.8$ nsec. The response to a single drifting electron is fast, but note that the time to collect the full charge is

$$t_{full} = (r_C^2 - r_A^2)\ell n(r_C/r_A)/2\mu V \approx 1.1 \text{ msec}$$

Integration times are generally much shorter than 1 msec in most experimental situations. For shorter integration times, T, the charge collected per ion pair produced by an ionizing particle will be

$$Q(T) = Ge\ \frac{\ell n(T/t_i + 1)}{2\ \ell n(r_C/r_A)}$$

and for $T = 10$ μsec, $Q(10\ \mu\text{sec}) \approx .6$ Ge for the parameters used above.

The number of ion pairs per millimeter of track length is approximately 4 in argon-based gases, and increases somewhat in more dense hydrocarbon gases. Fluctuations on this number may be quite large. The pulse formation from a track passing through a single cell will result from the ionization of electrons which drift in to the sense wire, avalanche, and in each case contribute a current $i(0)/(t/t_i+1)$ response. Ionization fluctuations, dispersion in electron arrival times, and avalanche (i.e., gain) fluctuations all contribute significantly to pulse fluctuations. Thus gas counters are intrinsically much more noisy amplifiers than are the scintillator or liquid argon readout systems. These fluctuations are reflected in the poorer energy resolution of gas sampling calorimeters. Figure 8 summarizes this discussion on pulse formation in proportional wire cells.

7. High Gas Gain

There are several advantages in operating gas sampling calorimeters in a high gas gain regime. There are also some disadvantages. Several regimes of operation have been identified and are referred to in literature. They include:

(i) Proportional mode: This regime is the lowest in gain, usually limited to $G \leq 5 \times 10^4$ where significant non-linearities or non-proportional performance sets in. The non-linearities are caused by space charge effects which limit the gain for higher charges deposited in the cell.

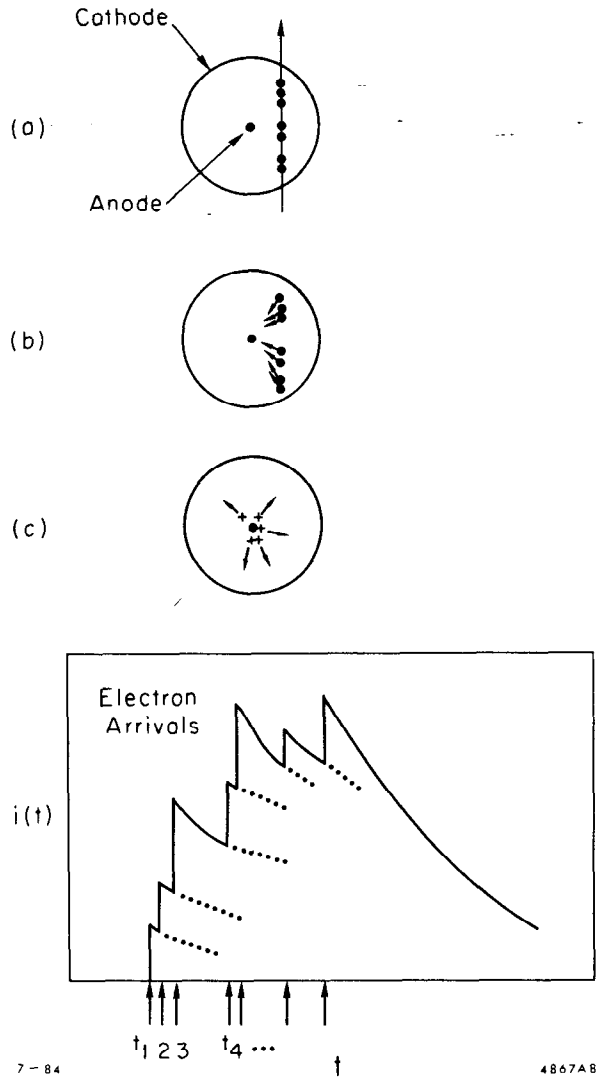

Figure 8. Pulse formation on an anode wire for cylindrical geometry is illustrated in three steps; (a) an ionizing particle track in a cell leaves electron-ion pairs in the gas; (b) electrons drift to the anode with velocities determined by the gas, electric fields, and pressure; (c) electrons undergo avalanche and gain with electrons collecting on the anode and positive ions drifting outward toward the cathode. The current pulse seen on the anode is the superposition of pulses from each electron arriving at the anode.

(ii) Saturated avalanche: At higher gains, $G > 10^5$, the ability for a pulse to grow in amplitude is strongly limited. In this regime, the charge deposition on anode wires becomes relatively independent of input charge due to the limiting mechanism. Thus the cell tends to produce a standard size pulse for a passing minimum ionizing particle. This mode is beneficial to gas calorimetry due to the reduced fluctuations.

(iii) Limited streamer mode: A higher gains in heavily quenched gases, large standard pulses will form for each passing track. These large pulses simplify the task for the preamplifier electronics. The pulses are digital in nature, and a simple system that counts the total number of pulses and measures the distribution of pulses works well. Energy resolution in this mode is comparable to that for saturated avalanche sampling counters. The large signals also lead to large induced cathode signals which are readily detected. Systems having conducting plastic cathodes with external pickup pads have been developed in Italy and Japan .

(iv) Geiger pulses, consisting of the entire anode wire breaking into a discharge, occur at higher gas gains in underquenched gases. This mode has been used for many years in Geiger tubes. Limiting the growth of the Geiger pulse by placing nylon fibers on sense wires achieves a digital gas readout similar to limited streamer mode devices, and achieves similar energy resolution.

Some experimental studies on how the mode of operation affects resolution in gas sampling calorimeters has been reported[13]. Operating a sampling device in the saturated avalanche or limited streamer modes offers an advantage in that large fluctuations in individual pulses can be limited. The contribution to the total signal from pulse fluctuations thus can be reduced. The philosophy in operating a gas calorimeter in the proportional mode is that the accumulated charge will be a good measure of energy. By operating in saturation, the hope is that the signal will have smaller fluctuations. Some detectors go to the extreme of operating in the Geiger region, limiting the growth of the Geiger pulses by fibers placed on the sense wires. In each of these modes, however, resolutions from $16\%/\sqrt{E}$ to $20\%/\sqrt{E}$ have been reported, and all techniques in the final analysis seem to work about equally well. Table II summarizes the results of different gas sampling electromagnetic calorimeters.

Figure 9 shows the performance properties of a prototype calorimeter for MAC[13]. The high voltages needed to drive that device into proportional, saturated avalanche, of limited streamer mode are shown. Figure 10 shows the corresponding resolution obtained for hadron interactions, versus voltage. The expected improvement in resolution is seen, having a minimum between saturated avalanche and limited streamer modes. Increasing the high voltage beyond these values worsened the observed resolution.

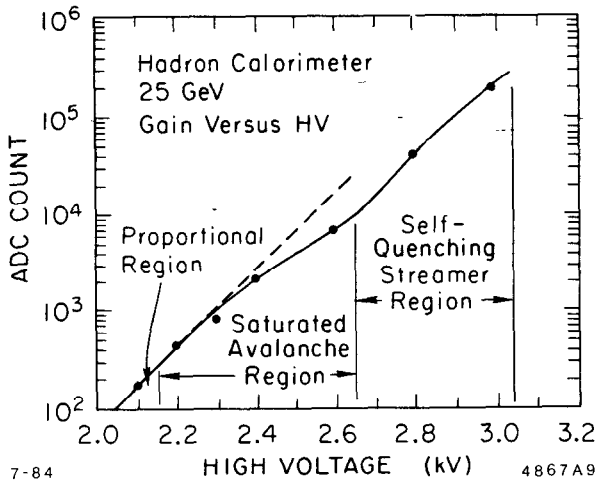

Figure 9. The gain (in units of ADC counts) versus high voltage in a MAC prototype test using argon-ethane-ethyl alcohol (49.3/49.3/1.4). Three regions of operation are identified (from Ref. 13).

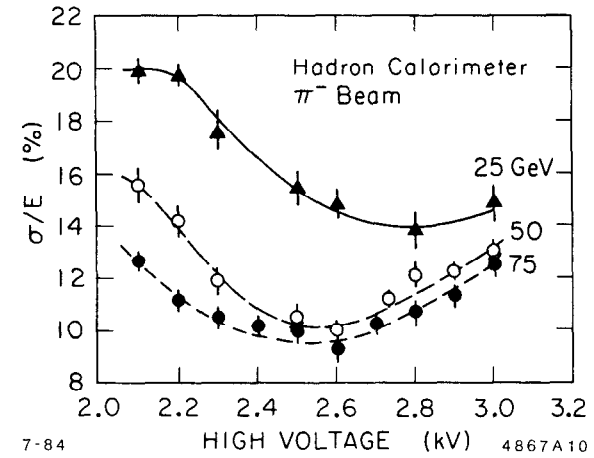

Figure 10. The resolution versus high voltage for the MAC prototype, for for three different energies of the incident π mesons (from Ref. 13).

8. Conclusions

The underlying physics of electromagnetic shower development is well understood. Analytic solutions of the complicated many body processes have been attempted with reasonable success, but modern day Monte Carlo computation yields the best numerical results. Experimental details may be inserted into the existing codes to study details such geometric effects.

Gas sampling calorimetry is the most economical and flexible system for large detectors of electrons, positrons, and photons. Resolution in energy is dominated by sampling fluctuations and pulse formation fluctuations. Typical systems approach $\sigma_E \approx .15\sqrt{E}$ in units of GeV, for sampling thicknesses of $\approx .5X_o$.

Advantages of operating gas sampling calorimeters at high gas gain exist. They include improved energy resolution and cheaper electronics.

References

1. B. Rossi, "High Energy Particles," Prentice Hall Inc., New York (1952), Chapter 2.
2. R. L. Ford and W. R. Nelson, "The EGS Code System: Computer Programs for The Monte Carlo Simulation of Electromagnetic Cascade Showers," SLAC-210 (1978).
3. D. F. Crawford and H. Messel, Phys. Rev. **128**, 2352 (1962).
4. H. H. Nagel and C. Schlier, Zeit. fur Physik **174**, 464 (1963).
5. D. F. Crawford and H. Messel, Nucl. Phys. **61**, 145 (1965).
6. H. H. Nagel, Zeit. fur Physik **186**, 319 (1965).
7. U. Vokel, DESY 67/16.
8. D. F. Crawford and H. Messel, "Electron Photon Shower Distribution Functions," Pergammon Press, New York (1970).
9. W. R. Nelson *et. al.*, Phys. Rev. **149**, 201 (1966).
10. C. A. Heusch and C. Y. Prescott, Phys. Rev. **135B**, 772 (1964).
11. A. Bauer *et. al.*, Proceedings of the Hamburg Conference, 401 (1965).
12. Y. Murata, *et. al.*, Proceedings of the Hamburg Conference, 417 (1965).
13. Proceedings of the Gas Calorimeter Workshop, Fermilab, October 1982.